International Journal of Hydrogen Energy 57 (2024) 789–797

Contents lists available at ScienceDirect

International Journal of Hydrogen Energy

journal homepage: www.elsevier.com/locate/he

Carbon Nanotubes (CNT) as an additive towards crack-free catalyst coated membranes (CCM)

Philipp Quarz *, Nadine Zimmerer, Anna-Maria Steck, Philip Scharfer, Wilhelm Schabel

Thin Film Technology (TFT), Karlsruhe Institute of Technology (KIT), 76131, Karlsruhe, Germany

ARTICLE INFO

Handling Editor: Shohji Tsushima

Keywords:
PEM fuel cells
PEM electrolyzers
Crack reduction
Membrane direct coating
CCM production
Electrode formation

ABSTRACT

In this study, carbon nanotubes (CNT) were used as an additive in coating inks for catalyst layers for PEM electrolyzers and fuel cells. Catalyst layers with and without CNT were prepared by direct membrane coating and analyzed for cracking behavior. The influence of CNT on crack prevention is discussed by varying the film thickness. Layers with CNT show no or less cracks at the same film thickness. Increasing the drying rate by raising the film temperature has no effect on crack formation, which allows shorter production times. The distribution and interaction of CNT in the microporous system are also discussed.

1. Introduction

The catalyst coated membrane (CCM) as key component of PEM electrolyzers and fuel cells consists of a membrane and two catalyst layers. During the production of the catalyst layers, (micro) cracks often occur in the layer. These cracks have an impact on system performance. The exact influence of cracks on performance and degradation is currently debated. Manahan et al. [1] observed crack-enhanced performance for fuel cells at high current densities and crack-induced lower performance at low current densities.

There are several reasons why cracks can affect performance. In a positive way, they improve mass transport properties during operation. The reactants diffuse more easily through the cracked structure and water in particular is better removed, allowing higher current densities on the cathode side [1,2]. On the other hand, product water can accumulate in the cracks, flooding the cell and reducing ionic and electrical conductivity [3,4].

Furthermore, cracks can act as a barrier to conduction processes by extending diffusion paths around the crack and reducing proton and electron conduction [4].

Cracks also influence mechanical properties of a system. During the production process and operation, the membrane swells and shrinks continuously, leading to tensions within the system [5,6]. Catalyst-free areas (in-plane defects) in the CCM react differently to these moisture-induced dimensional changes compared to catalyst-covered areas [7]. Those tension differences respective the ability to handle them differently can stress the membrane and lead to pinholes and cracks not only in the catalyst layer but in the membrane itself [4,8,9]. These defects increase during operation and can cause larger defects such as cracks and new defects as delamination between the membrane and catalyst layer [10–13].

At defective areas in the catalyst layer, the local gas crossover is increased, which can further damage these areas through e.g. the potential formation of H_2O_2 [11]. This in the end will lead to mixing potentials and loss of fuel and therefore to a degrading performance. Moreover, it also reduces the lifetime of the devices [11,14].

In high temperature fuel cells, phosphoric acid can migrate through cracks. Cracks in the catalyst layer are injection points for the flooding of the microporous layer and the gas diffusion layer [15,16].

Since cracks have some positive and many negative effects on cell performance, an optimal ratio of cracks to total catalytic area can be postulated [17]. Nevertheless, the negative influences of cracks appear to predominate. Thus, the aim is to avoid cracking in catalyst layers. To achieve this, it is necessary to understand and control the formation of cracks.

A promising approach is to do this with additives, for which carbon nanotubes (CNT) are suitable due to their special properties. The addition of CNT reduces crack formation and improve long time performance [18,19].

CNT are cylindrical tubes, based on graphene which is sp^2-

* Corresponding author.
E-mail address: philipp.quarz@kit.edu (P. Quarz).

https://doi.org/10.1016/j.ijhydene.2024.01.049
Received 22 September 2023; Received in revised form 7 December 2023; Accepted 3 January 2024
Available online 13 January 2024

hybratizised carbon forming an atomic hexagonal honeycomb pattern. The tubes have a diameter in the nanometer scale and an axial size ranging from 1 μm to a few centimeters. A distinction is made between Single Wall Carbon Nano Tubes (SWCNT) and Multiwall Carbon Nano Tubes (MWCNT) [20]. In addition, depending on the structure, armchair, chiral, and zigzag modification, described by a pair of indices (n,m), can be distinguished. This results in different properties such as metallic or semiconducting electrical behavior [21].

In general, CNT have a high mechanical stability, in particular a high shear modulus. They respond elastically to axial loads and also have good electrical conductivity [22].

In addition, CNT can be used in electrolyzer and fuel cell electrodes as platinum-doped carrier particles. In this case, the CNT improve the performance of the catalyst, increase the stability and corrosion resistance of the catalyst and allow savings on the expensive platinum catalyst and overall costs due to the improved catalytic properties [19,23].

2. Formation of cracks

One reason for cracking is the pressure difference in pores of different sizes. During drying, solvents evaporate and catalyst particles approach each other. The film shrinks until the final film thickness is reached and a pore network filled with solvents is formed. As the pore network is emptying as drying progresses, capillary pressure develops within the pores in the partly dried catalyst layer. In this process, large pores empty faster than small ones. This results in stresses in the pore network that can result in micro-cracks [24], which can later develop into macro-cracks. Suzuki et al. [25] postulate that these micro-cracks are prevented by the addition of CNT to fuel cell inks. Instead, macro-pores are formed, which cause lower stresses in the pore network.

The effects of capillary pressure on crack formation can be explained by fracture mechanics and a critical crack stress σ_c can be determined using Griffith's criterion [26]. Tirumkudulu et al. [27] extended the model and define a dimensionless critical stress for an isolated crack to the dimensionless film thickness (1).

$$\frac{\sigma_c r}{2\gamma_L} = 0.1877\left(\frac{2r}{h_c}\right)^{\frac{2}{3}}\left(\frac{GM\varphi_{rcp} r}{2\gamma_L}\right)^{\frac{1}{3}} \quad (1)$$

The layer height h_c, the surface tension of the solvent γ_L and the shear modulus G are considered. The particle radius r has no influence, it serves to transform into a dimensionless parameter. The shear modulus is directly related to the elastic modulus. Since the calculation of σ_c is only related to a single location in the layer, the dimensionless quantities M (for the number of particles in contact at this location) and φ_{rcp} (for the volume fraction of particles affected at this particular location in the layer) are included.

Singh et al. [28] derive from equation (1) an expression for the critical crack thickness h_c (CCT), which gives an indication of the height up to which the layer is resistant to cracking (2). In this equation, the maximum capillary pressure p_{max} affecting the layer is considered.

$$h_c = 0.64\left(\frac{GM\varphi_{rcp} r^3}{2\gamma_L}\right)^{\frac{1}{2}}\left(\frac{2\gamma_L}{p_{max} r}\right)^{\frac{3}{2}} \quad (2)$$

I.e., h_c is proportional to $G^{\frac{1}{2}}$, $M^{\frac{1}{2}}$, $\varphi_{rcp}{}^{\frac{1}{2}}$, to γ_L and anti-proportional to $p_{max}{}^{\frac{3}{2}}$. The addition of elongated CNT (increasing M and φ_{rcp}) with high G-modulus is expected to increase the CCT. While the surface tension of the solvent remains unaffected, CNT addition could change the capillary pressure due to minor variations in the resulting pore sizes or contact angles. However, these changes should be significantly smaller than the increases in G, M and φ_{rcp}, which dominate.

Kumano et al. [29] determined the CCT experimentally for catalyst layers for fuel cell applications with varying layer thicknesses (LT). For the system used, they were able to specify a CCT, before which no primary cracks occurred, of approx. 3 μm and 11 μm depending on ink formulation. Hoffmann et al. [30] define a CCT not from the occurrence of the first crack, but from a critical value at which 1 % of the layer surface is cracked. With different platinum-free carbon black particles they determined the CCT experimentally between 10 μm and 30 μm. The CCT can vary within a layer due to inhomogeneous distributions of ionomer and particles [31].

Due to the promising mechanical properties of CNT, this study investigates to what extent they can be used in catalyst layers as an additive for crack prevention. Cracks form after coating the catalyst ink and during film solidification. Hereby, ink formulation and drying conditions have an influence on crack formation.

In fuel cell and electrolyzer coating inks, a higher ionomer to carbon ratio, regardless of its effect on cell performance [32], results in fewer cracks and increases the CCT [30]. In addition, the particle morphology [30] as well as the solvent (mixtures) used and thus their respective interaction with the ionomer have an influence on the formation of cracks in drying catalyst layers [29,33–35].

Besides the ink formulation, ink processing and resulting particle size distribution also influence crack formation [36]. The membrane direct coating also has an effect on the occurrence of cracks, as the membrane swells and shrinks in contact with the solvent-based ink [34]. In addition, the drying conditions can also influence crack formation. In the case of inks based on solvent mixtures, selective drying usually occurs, resulting in changes to the formulation during processing. Here, drying conditions such as flow control, heat transfer coefficient, temperature and water humidity or preloading of the drying air have a major influence [37,38].

3. Material and methods

3.1. Ink production

Catalyst powder TEC10EA50E with 46 wt% platinum (TANAKA Kikinzoku Kogyo K.K., Japan) and Multiwall Carbon Nanotubes (MWCNT, Sigma-Aldrich Chemie GmbH, Germany) in different mass fractions were mixed with Nafion™ D2020 (Chemours, USA), ultrapure water (Milli-Q® EQ 7000, Merck, Germany) and 1-propanol (Carl Roth GmbH, Germany). The overall solvent mixture of water to 1-propanol was 80:20 wt%. The ionomer to carbon ratio (I/C) by weight based on the carbon content of the inks without CNT was set to 1.0. The total amount of ionomer was constant in the different inks, as well as the solid content at 10 wt%.

The increasing CNT content from 0, 1, 3 and 5 wt% of the solids content was adjusted at constant solid weight of 10 wt% and thus by reducing the catalyst content (Table 1). Since the CNT consist of carbon, this effectively also changes the I/C ratio, but only slightly. Inks were produced in a ball mill CN 10, APS 250 (VMA Getzmann GmbH, Germany, 3 h at 1000 rpm) containing grinding media made of yttrium stabilized zirconium oxide.

3.2. Ink characterization

The particle sizes of the inks were determined by dynamic light

Table 1
Catalyst ink formulations with increasing CNT content in wt%. Solid content is 10 wt%, so resulting layers have a CNT fraction of 0 (A), 1 (B), 3 (C) and 5 wt% (D).

	A	B	C	D
CNT	0.0	0.1	0.3	0.5
Catalyst	6.5	6.4	6.2	6.0
Nafion™	3.5	3.5	3.5	3.5
1-propanol	18.0	18.0	18.0	18.0
Water	72.0	72.0	72.0	72.0

scattering (Mastersizer 3000, Malvern Panalytical, UK). As it is the main solid component, the refractive index of carbon black ($n_{CB} = 1.746$ [39]) was used for the particles. Platinum, ionomer and CNT could influence the refractive index. This would cause the curves to shift slightly. Qualitative comparability is given. Inks were diluted in an ultrasonically degassed solvent mixture ($n_{solvent} = 1.34$) with a water and 1-propanol mass fraction ratio of 80:20 wt%.

3.3. Coating and drying of the catalyst layers

The inks were coated directly on a Nafion™ N212 membrane (Chemours, USA) using a doctor blade ZUA 2000 (Zehntner-Testing-Instruments, Switzerland). The coating gap varied from 75 µm to 225 µm to achieve different wet film thicknesses. The catalyst film was dried with a combination of contact drying and convective drying, adjusting isothermal conditions [40–52]. The isothermal drying temperature was set to 25 °C, 35 °C and 45 °C and the heat and correlated mass transfer coefficient was set constant in the drying channel to a fixed and adjusted value of 35 W/(m^{2}K).

3.4. Analysis of the catalyst layers

The film thickness was determined using a digital dial gauge (ID-H0530, Mitutoyo Japan). The occurrence of cracks was studied by backlit images of the layers. As the light passes through the defects, they appear white, while the coating appears black [31]. Images are converted to a binary bitmap and analyzed using the software 'ImageJ'. A digital microscope VHX-7000 (Keyence, Japan) was used for microscope images and a Zeiss Supra 55 (Carl Zeiss AG, Germany) for SEM investigations. First four-point in-plane conductivity measurements were done (3 cm × 3 cm sample size) using an E3633A power supply (Agilent Technologies, USA) and a multimeter (2700 Keyence, Japan).

4. Experimental results

4.1. Ink properties

Ink properties and in particular the particle size distribution of the catalyst influence the resulting layers. All inks show similar bimodal particle size distributions (Fig. 1). The fine fraction is under approx. 90 nm and represents the primary particles. The second peak representing agglomerates lies in the area between 100 nm and the maximum particle size measured below 2 µm. This is particularly important for the quality of the catalyst layers, since agglomerates are often origin for defects.

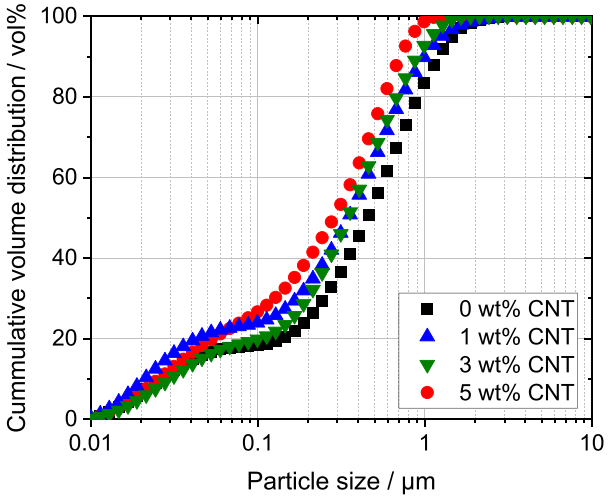

Fig. 1. Particle size distribution (PSD) of coating inks with increasing CNT mass fraction from 0 to 5 wt%. The CNT data refer to the solid content. In the total ink, the proportion is lower by a factor of 10. CNT particles have a magnitude of ~0.1 µm.

The inks with CNT all have a slightly increased fine fraction in the order of 0.1 µm compared to the CNT-free ink. Including manufacturer's specifications, this increase can be attribute to the CNT (CNT diameter: 50–90 nm [53]).

4.2. Crack formation in catalyst layers

At constant drying parameters, the influences of film thickness and CNT content on the crack pattern in the membrane direct coatings get obvious. For this purpose, the formed structures of the four formulations with different CNT content are first compared optically at comparable dry film thicknesses (4, 8, 10, >10 µm). At the given composition and porosities around 53 % (without CNT), 4 µm layer thickness (LT) corresponds to a calculated platinum loading of approx. 0.17 mg$_{Pt}$/cm^2, 8 µm to approx. 0.34 mg$_{Pt}$/cm^2 and at 10 µm to approx. 0.42 mg$_{Pt}$/cm^2. These values can be only an orientation e.g. due to derivations in the porosities. The platinum loading of the catalyst layer reduces by around 2.5 % if 1 wt% CNT is added to the catalyst and Nafion. In general, with a targeted platinum loading of the layer, the particle loading, the layer composition and the porosity influence the desired or necessary film thickness. If the layer loading should remain the same, a lower platinum content in the particles or a higher layer porosity requires thicker layers.

The nomenclature of the layers is derived from the CNT content of the layer (0 wt% ≙ A, 1 wt% ≙ B, 3 wt% ≙ C, 5 wt% ≙ D) and the corresponding LT in µm. For example, A4 describes the layer with 0 wt% CNT and 4 µm thickness. Defects of the layer are visible as white areas in backlight (Fig. 2).

Based on an ink without CNT, the influence of the LT is first discussed. The fraction of defects increases as the LT increases from the left to the right (Fig. 2). At 4 µm (A4), numerous but still small point-like defects can be seen. At 8 µm, they are already larger (A8) and at 10 µm clearly formed cracks (A10). At targeted LT greater than 10 µm, spalling no longer causes a continuous layer to form, which also limits the determination of the LT (AX).

Typical examples for defect types occurring in PEM catalyst layers can be seen at different LT of the ink without CNT (Fig. 3). The defects in Fig. 2, which appear partially point-like (A4), can be identified as (short) cracks under the microscope (Fig. 3, A4). In some cases, agglomerates and other inhomogeneities in the layer are the origin for crack formation. Fig. 3, A4 shows small cracks under 40 µm which are randomly oriented around an inhomogeneity.

At greater thicknesses, individual, clearly pronounced primary cracks form. Branching off from these, the first smaller secondary cracks also develop (A8). With further increasing LT, larger cracks occur, which partially coalesce (A10). This can subsequently lead to the formation of a crack network or spalling and delamination effects.

The layers' defect area relative to the total area increases from approx. 2 % at a LT of 4 µm, to 14 % (8 µm) and 22 % (10 µm). More defect area than layer is observed when the thickness exceeds 10 µm (Fig. 4, black). The number of defects instead decreases from approx. 14,400 (4 µm) to 12,900 (8 µm) to 8300 (10 µm) (Fig. 4, purple). This is due to coalescence of the defects. In combination, the average size of the defects increases with LT.

4.3. Influence of CNT on crack formation

Regarding the effects of film thickness, the influence of CNT on the crack pattern is discussed at constant film thicknesses, first at 4 µm (Fig. 5). If CNT are added to the catalyst ink (B4, C4, D4), the defect fraction of the layers decreases. Despite the somewhat less favorable I/C ratios, there is a slight tendency towards a smaller defect area with increasing CNT content.

The trend is more pronounced with higher film thicknesses. This is particularly evident at a LT of 8 µm (Fig. 6). Without CNT (A8), many

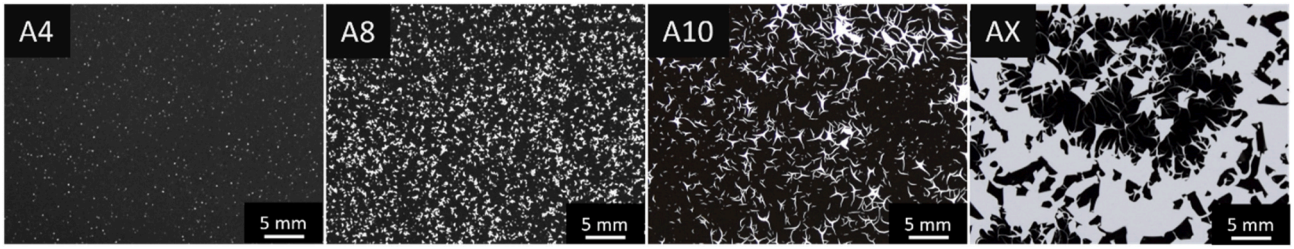

Fig. 2. Influence of the layer thickness (LT) on catalyst pattern. Conventional inks without CNT (A) were coated directly on the membrane and dried under constant drying conditions with 25 °C film temperature and a heat transfer coefficient of 35 W/(m^{2}K). Defects are shown in white. The defect fraction increases with increasing LT. Targeting LT greater than 10 µm, spalling occurred and the film thickness could not be determined (AX).

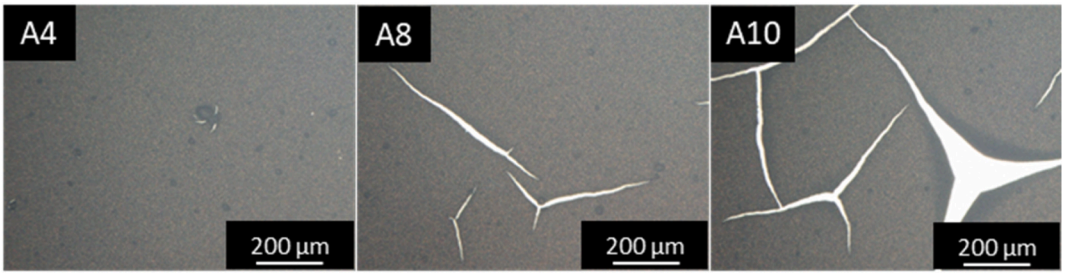

Fig. 3. Microscope images of layer thicknesses (LT) at 4 µm (A4), 8 µm (A8) and 10 µm (A10) without CNT (index A). Observations: defect areas become larger. Different cracks combine and form one large defect (A10).

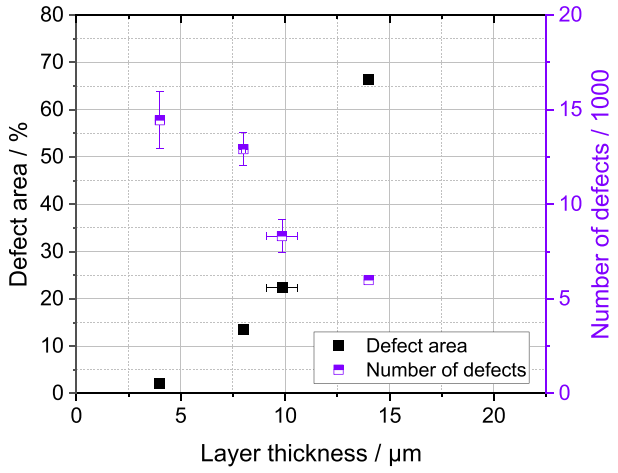

Fig. 4. Percentage of defects (cracks, spalling, etc.) relative to the total area of the CNT-free membrane direct coatings (black) and number of defects (purple) vs. the film thickness. Films were dried at an isothermal film temperature of 25 °C and a heat transfer coefficient of 35 W/(m^{2}K). With increasing thickness, the defect fraction increases while the number of defects decreases. This results from crack coalescence. (For interpretation of the references to colour in this figure legend, the reader is referred to the Web version of this article.)

cracks are present. Their proportion is lower at 1 wt% CNT content (B8) and merges into a few rather point-like defects at 3 wt% (C8). With 5 wt % (D8), hardly any defects can be detected.

When plotting the defect area fraction over the dry LT, the trend towards more defect area with thicker layers is clearly visible for all studied catalyst layers (Fig. 7). As the CNT fraction increases, the defect area decreases at the same LT. Already at a thickness of 4 µm, the defect percentage without CNT is more than twice as high (2 %) as for the ink with 1 wt% CNT (0.8 %). At 8 µm, the defect area decreases with increasing CNT content from 13.5 % to 3.2 %–0.9 % and finally to 0.01 %.

Same effects are visible for LT of 10 µm. The catalyst layer with 5 wt % CNT at 11 µm still shows nearly no cracks.

Targeting more than 10 µm LT, the coatings without and with 1 % CNT content show larger spalling from the membrane. In contrast, the films with 3 wt% and 5 wt% outperform. To find out the extremes, LT greater than 20 µm were targeted for the stable formulations with 3 wt% and 5 wt% CNT. Thus, with 3 wt% CNT at 22.5 µm, a layer appearance is obtained which was already reached at 10 µm with the ink without CNT. The layer with 5 wt% CNT still shows a defect-free appearance at a thickness of 21.3 µm apart from a few flakes.

The defect fractions of the layers with CNT are all closer together than those without CNT. In summary, it can be stated that even small amounts of CNT significantly improve the layer appearance.

Following Hoffmann et al. [30], the CCT is defined here as the LT at which the cracks account for more than 1 % of the total catalyst area. For the ink without CNT, the CCT is already exceeded at 4 µm. For the formulation with 1 wt% CNT, the CCT is between 4 and 8 µm and for the formulations with 3 and 5 wt% it is above 10 µm. The CNT increase the CCT.

Suzuki et al. [25] suggest the formation of macro-pores by adding CNT to counteract the formation of micro-cracks in the catalyst layers. Taking equation (1) into account, the addition of the highly stiff CNT increases the shear modulus G via the large elastic modulus and has a positive effect on the CCT. Meanwhile, the elongated shape of the CNT also increases the number of contacting neighbors M, also leading to a higher CCT. The combination of round particles and space-occupying fibrous CNT results in a quasi-composite material that can withstand higher forces and stresses.

In addition to the size of the defective areas, the number of defects can be analyzed. As is obvious, there are always more defects in the coatings without CNT than in those with, regardless of the coating thickness (Fig. 8). At 4 and 8 µm thickness, the layers without CNT reveal about twice as many defects as the ink with 1 wt% and about 3 times as many as the 3 wt% CNT layer. In the layer with 5 wt% CNT there are only a few, single defects.

As the LT increases, the number of defects decreases for all formulations. This can be explained by the formation of a crack network where small (primary) cracks grow and coalesce to bigger ones. Large crack networks pose the risk of delamination of the catalyst from the

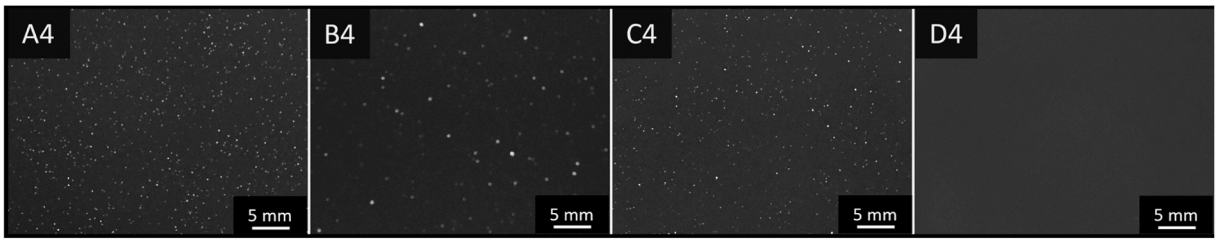

Fig. 5. Influence of the CNT content on catalyst pattern. Layers containing 0 (A), 1 (B), 3 (C) and 5 wt% CNT (D) were coated directly on the membrane and dried under constant drying conditions with 25 °C film temperature and a heat transfer coefficient of 35 W/(m^{2}K). Defects are shown in white. An increase in the CNT content reduces the defect content for the same film thickness (here LT = 4 µm).

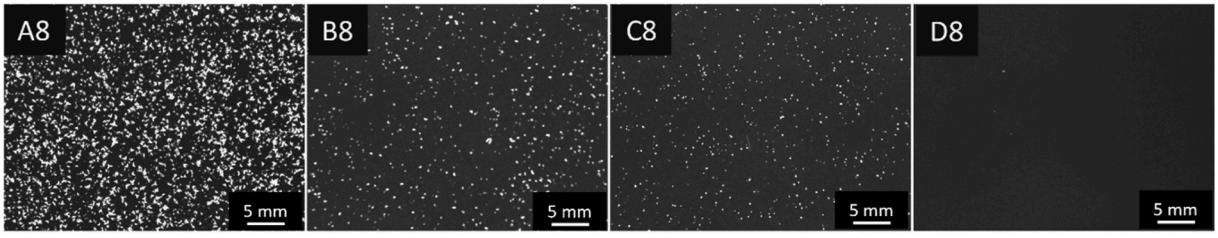

Fig. 6. Influence of the CNT content on catalyst pattern. Layers containing 0 (A), 1 (B), 3 (C) and 5 wt% CNT (D) were coated directly on the membrane and dried under constant drying conditions with 25 °C film temperature and a heat transfer coefficient of 35 W/(m^{2}K). Defects are shown in white. An increase in the CNT content reduces the defect content for the same film thickness (here LT = 8 µm).

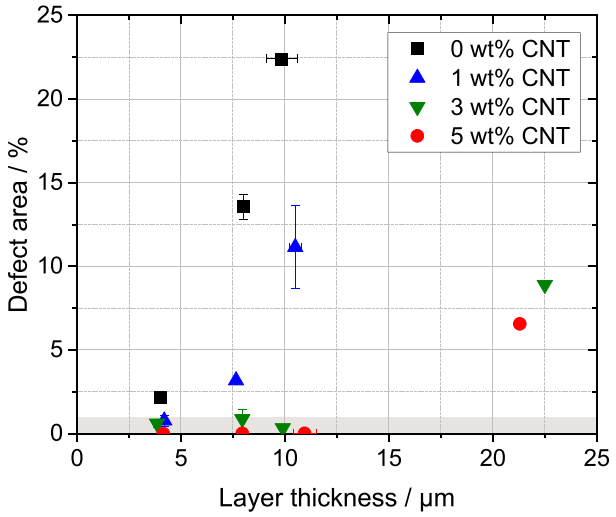

Fig. 7. Percentage of defects (cracks, spalling, etc.) relative to the total area of the membrane direct coatings over the film thickness. Films with 0 wt% (black), 1 wt% (blue), 3 wt% (green) and 5 wt% (red) were dried at an isothermal film temperature of 25 °C and a heat transfer coefficient of 35 W/(m^{2}K). With increasing thickness, the defect fraction increases. A higher CNT content reduces the defect content per film thickness. At 10 µm, the layers with 3 wt% and 5 wt% CNT show almost no defect area. (For interpretation of the references to colour in this figure legend, the reader is referred to the Web version of this article.)

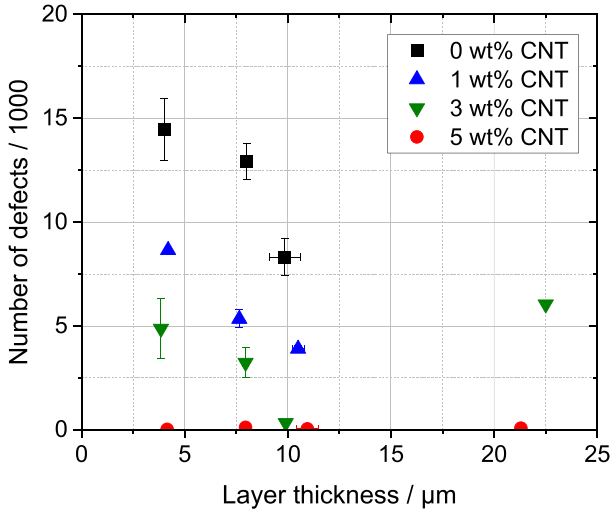

Fig. 8. Number of defects (cracks, spalling, etc.) vs. the layer thickness (LT). The number of defects decreases with increasing thickness due to crack coalescence. A comparison of direct membrane coatings of the same thickness shows a decreasing number of defects with increasing CNT content from 0 wt% (black), via 1 wt% (blue), via 3 wt% (green) to 5 wt% (red). Layers with 5 wt% show almost no defects independent of LT. All inks were dried at 25 °C isothermal film temperature and a heat transfer coefficient of 35 W/(m^{2}K). (For interpretation of the references to colour in this figure legend, the reader is referred to the Web version of this article.)

membrane and the formation of insurmountable charge transport resistances and thus performance losses. The goal should therefore initially be to avoid these (large) defects.

Regardless of the formulation, the average defect size is similar at 4 µm thickness (4–7 µm^2). Thereafter, as can be concluded from Figs. 7 and 8, it increases with increasing LT. As long as no spalling occurs, the average sizes of the CNT-free layers are larger than those with CNT. For example, at 8 µm, the average defect size in the CNT-free layer is about 70 µm^2, twice that of the 1 wt% CNT coatings. With increasing CNT content, the average defect size decreases.

Furthermore, CNT postpone the formation of defect types discussed in Fig. 3 (short, point-like cracks; primary cracks; coalescing cracks, crack network, spalling), to higher LT. At 8 µm, point-like defects occur in the 3 wt% CNT-containing layer. Without CNT, there are several cracks and they are about to coalesce (Fig. 9). In terms of defect type, C8 is more comparable to the half-thick A4 in Fig. 3.

The extent of the cracks influences the properties of the catalyst layers. First in-plane conductivity measurements for the layer without

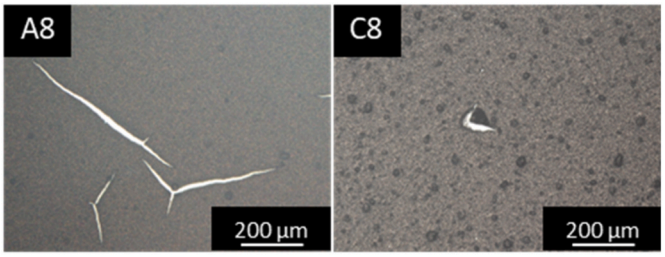

Fig. 9. At similar layer thickness (LT = 8 µm), pronounced cracks in the coating without CNT (A8) result in higher defect areas than the more point-like cracks in the layer with 3 wt% CNT (C8).

CNT (A8) show values around approx. 460 S/m ± 23 S/m, comparable to values listed in Ref. [54]. With 1 wt% and 3 wt% CNT, the conductivity increases by about 23 %. With 5 wt% CNT, it is approx. 2.8 times higher than without CNT. The increase in conductivity is presumably due to the good conductivity of the CNT themselves, but especially due to the significantly fewer defects and thus the shorter diversions. This is in principle advantageous for the addition of CNT with regard to potential performance data. In general, however, further investigations, especially on performance data, must be conducted in this direction.

4.4. Influence of higher drying temperatures

To achieve shorter production times, faster drying is interesting for the commercial fabrication of catalyst layers. One way to reduce the drying time is via increasing the drying rate by increasing the isothermal film drying temperature [40,41,52,55]. Increasing this from 25 °C to 35 °C and 45 °C corresponds to an initial drying rate of about 1.2, 2.2 and 3.9 g/(m^{2}s) assuming selective evaporation and therefore accelerates drying by a factor of 1.7 and 3.2 (calculated using heat and mass balances of 1-propanol/water mixtures). Higher film thicknesses due to higher wet film thicknesses have no influence on the (initial) drying rate, but extend the overall drying time [44,56].

Fig. 10 shows 4 µm thick coatings with 0 wt% (A) and with 3 wt% CNT content (C), dried at 25 °C, 35 °C and 45 °C at a constant heat transfer coefficient of 35 W/(m^{2}K). In the nomenclature, the film drying temperature is supplemented deviating from 25 °C with 35 at 35 °C and 45 at 45 °C.

As already seen above, layer containing CNT have less defects than ones without for each observed drying temperature (C to A).

Considering the same conditions (LT and CNT content), an increased film drying temperature has no influence on the crack pattern of the formulations studied. Thus, the main influencing factors for crack formation in catalyst layers are the LT and the mass fraction of CNT here. It is shown that catalyst layers can be dried 1.7 and 3.2 times faster, without obtaining negative effects on crack formation.

The optical impressions of the catalyst layers investigated by back illumination can be supported by image analysis. Fig. 11 shows that the defect area fraction is approx. constant for all four formulations, when the drying rate is increased. At 4 µm thickness, the films without CNT have a defect area fraction of about 2 %. Meanwhile, the defect fraction for the films with CNT are 0.4 % (1 wt% CNT), 0.4 % (3 wt% CNT), 0.02 % (5 wt% CNT). All catalyst layers with CNT therefore have a crack area below 1 %, the critical value for CCT defined here. There is no discernible trend in the number of defects, the average defect size and the defect orientation depending on the film drying temperature.

Same observations can be made for other LT with higher defect fractions. Also at 8 µm, there is no influence of the increased drying temperature on crack pattern visible (Fig. 12).

4.5. Microstructure of catalyst layers with CNT

A closer look at the microstructure in cross-section (CS) and

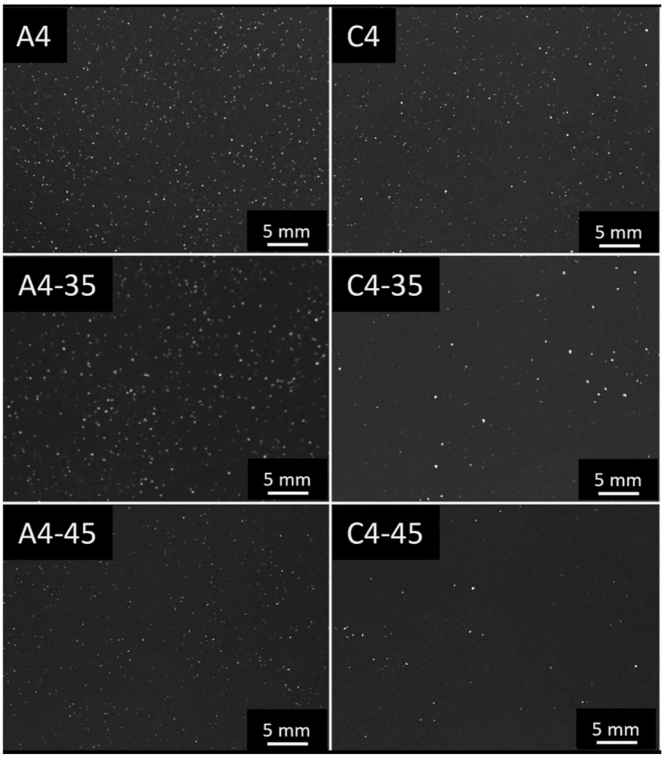

Fig. 10. Influence of the isothermal film drying temperature on the film appearance of selected films. Direct membrane coatings without (A) and with 3 wt% CNT content (C) are shown at 4 µm thickness. An increase from 25 °C to 35 °C and 45 °C and the associated increase in drying rate and shorter drying time do not lead to a significant change in the appearance per column. Heat transfer coefficient was fixed at 35 W/(m^{2}K) and dew point comparable for all trials.

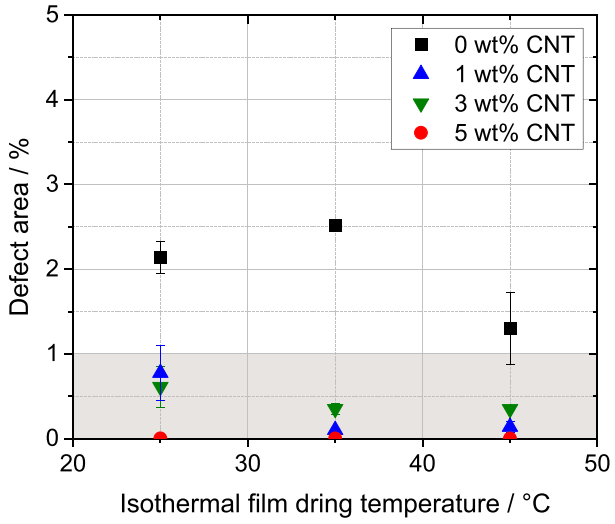

Fig. 11. Defect area of coatings of 4 µm height and CNT contents of 0 wt% (black), 1 wt% (blue), 3 wt% (green) and 5 wt% (red) versus increasing film temperature during drying. With increasing film drying temperature and the associated higher drying rate respectively shorter drying time, the defect percentage does not change significantly for the formulations investigated. The inks with CNT are all below a defect fraction of less than 1 % of the area considered and thus the coatings below the critical crack thickness (CCT). (For interpretation of the references to colour in this figure legend, the reader is referred to the Web version of this article.)

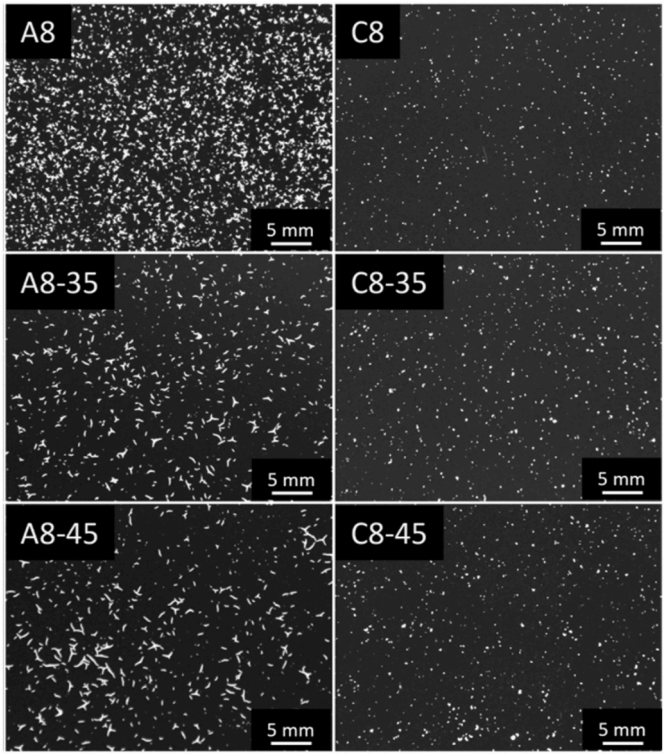

Fig. 12. Influence of the isothermal film drying temperature on the film appearance of selected films. Shown are direct membrane coatings without (A) and with 3 wt% CNT content (C) at 8 µm thickness. An increase from 25 °C to 35 °C and 45 °C and the associated increase in drying rate and shorter drying time do not lead to a significant change in the appearance per column. Heat transfer coefficient was fixed at 35 W/(m^{2}K) and relative humidity comparable for all trials.

untreated top view (TV) of the coatings provides information about the distribution of the CNT. The effective structure is the link to the subsequent performance of the electrodes. In the SEM images the CNT can be seen as elongated filaments next to the small roundish catalyst particles (Fig. 13, D). Their length of several µm compared to the catalyst particles (primary diameter: 50 nm, manufacturer's specification) is clearly visible. At the same time, they are embedded into the porous catalyst network. There does not seem to be a preferred orientation.

In Fig. 13, D-CS1, one of very few occurring partial cracks, which means no crack propagation to the membrane, can be seen. These types of cracks are not visible when viewed with back illumination. It looks like some CNT are connecting both sides of the crack like bridges. This probably prevented further tearing.

The partial cracks occur only very sporadically and are observed only in CNT-containing layers. The reason for this could be that the partial cracks in layers without CNT propagate directly to the membrane. An example of a crack going through the whole catalyst layer to the membrane, typical for the CNT-free coatings, is shown in Fig. 13, A-CS1. Around the crack, partial delamination between the layer and the membrane is observed, as predicted in e.g. Refs. [12,13]. This is suggested to be a negative aspect of cracks according to CCM performance and lifetime.

CNT generally inhibit the formation of cracks and could stabilize emerging ones forming resilient bridges. Relevant to operation, these CNT bridges could continue to enable charge transport across a partial crack.

5. Conclusion

Catalyst inks with different carbon nanotube (CNT) contents were produced in a ball mill. They showed a similar particle size distribution with an elevation around 100 nm, where the CNT can be categorized to. After membrane direct coating and isothermal drying, the defect area of the coated layers increases as the layer thickness (LT) increases.

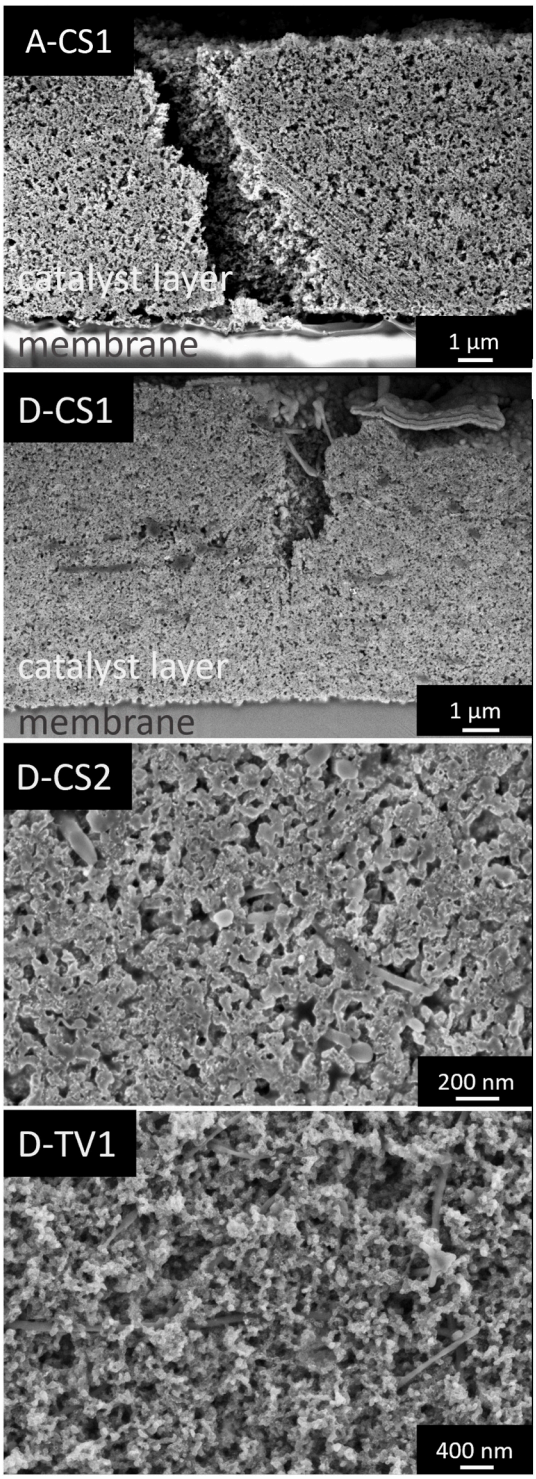

Fig. 13. SEM images of the cross section (CS) of a CNT-free layer showing a crack and partial delamination (A-CS1) as well as cross section (D-CS1 & D-CS2) and top view (D-TV1) of a layer containing 5 wt% CNT (index D). The scaling bar resolutions are 1 µm, 0.2 µm and 0.4 µm. The CNT can be identified as elongated threads that are woven into the porous catalyst particle-ionomer network. Isolated partial cracks are observed in CNT-containing layers. It seems that some CNT stretch across them (D-CS1).

Meanwhile, the number of defects decreases as cracks coalesce.

Catalyst layers containing CNT show crack areas lower than 1 % even at high LT. At same LT, layers containing (more) CNT show less defects. With increasing CNT content the critical crack thickness (CCT) increases. The positive effect of CNT prevails the effect of a slightly lower I/C in the inks. With 5 wt% CNT it is possible to produce a 10 μm thick catalyst layer coated directly on the membrane with nearly no defects.

CNT are distributed homogeneously in the porous layer. It results a quasi-composite material. In an observed partial crack, they stretch like a bridge across the crack and fix it. It is hypothesized that CNT can act as bridges within the catalyst layer which stabilize emerging cracks and additionally could maintain electron conduction across cracks.

Catalyst inks were dried at higher drying rates to increase production throughput (isothermal film temperatures at 25, 35 and 45 °C). Independent of the higher drying rates in form of the higher film temperatures, the defect formation was not influenced by the drying conditions. Therefore, it was possible to produce nearly defect-free catalyst layers coated directly on the membrane with an initial drying rate of 3.9 g/(m^2s).

First in-plane conductivity measurements show a higher conductivity within the catalyst layers with increasing CNT and coupled decreasing defect fraction. In the future, the influence of CNT and drying conditions, and especially the influence of defects on the electrochemistry and performance of CCM, should be further investigated.

Declaration of competing interest

The authors declare that they have no known competing financial interests or personal relationships that could have appeared to influence the work reported in this paper.

Acknowledgements

The authors would like to thank Marcus Müller from the Institute for Applied Materials (IAM) – Energy Storage Systems (ESS), Karlsruhe Institute of Technology (KIT), 76144 Eggenstein-Leopoldshafen, Germany for performing the SEM images.

References

[1] Manahan MP, Kim S, Kumbur EC, Mench MM. Effects of surface Irregularities and Interfacial cracks on polymer electrolyte fuel cell performance. ECS Trans 2009;25(1):1745–54. https://doi.org/10.1149/1.3210730.
[2] Markötter H, Haußmann J, Alink R, Tötzke C, Arlt T, Klages M, et al. Influence of cracks in the microporous layer on the water distribution in a PEM fuel cell investigated by synchrotron radiography. Electrochem Commun 2013;34:22–4. https://doi.org/10.1016/j.elecom.2013.04.006.
[3] Schmittinger W, Vahidi A. A review of the main parameters influencing long-term performance and durability of PEM fuel cells. J Power Sources 2008;180(1):1–14. https://doi.org/10.1016/j.jpowsour.2008.01.070.
[4] Kundu S, Fowler MW, Simon LC, Grot S. Morphological features (defects) in fuel cell membrane electrode assemblies. J Power Sources 2006;157(2):650–6. https://doi.org/10.1016/j.jpowsour.2005.12.027.
[5] Ma L, Zimmerer N, Schäfer J, Quarz P, Heckmann T, Scharfer P, et al. Investigation on a micro-environment concept for MEA production process supported by numerical simulations. December 06, 2023. Available from: https://nbn-resolving.org/urn:nbn:de:bsz:ch1-qucosa2-764450.
[6] Sadeghi Alavijeh A, Bhattacharya S, Thomas O, Chuy C, Yang Y, Zhang H, et al. Effect of hygral swelling and shrinkage on mechanical durability of fuel cell membranes. J Power Sources 2019;427:207–14. https://doi.org/10.1016/j.jpowsour.2019.04.081.
[7] Goulet M-A, Arbour S, Lauritzen M, Kjeang E. Water sorption and expansion of an ionomer membrane constrained by fuel cell electrodes. J Power Sources 2015;274:94–100. https://doi.org/10.1016/j.jpowsour.2014.10.040.
[8] Singh Y, Khorasany RMH, Kim WHJ, Alavijeh AS, Kjeang E, Rajapakse RKND, et al. Ex situ characterization and modelling of fatigue crack propagation in catalyst coated membrane composites for fuel cell applications. Int J Hydrogen Energy 2019;44(23):12057–72. https://doi.org/10.1016/j.ijhydene.2019.03.108.
[9] Ding G, Santare MH, Karlsson AM, Kusoglu A. Numerical evaluation of crack growth in polymer electrolyte fuel cell membranes based on plastically dissipated energy. J Power Sources 2016;316:114–23. https://doi.org/10.1016/j.jpowsour.2016.03.031.
[10] Alavijeh AS, Khorasany RMH, Nunn Z, Habisch A, Lauritzen M, Rogers E, et al. Microstructural and mechanical characterization of catalyst coated membranes Subjected to in situ Hygrothermal fatigue. J Electrochem Soc 2015;162(14):F1461–9. https://doi.org/10.1149/2.0471514jes.
[11] Arcot MP, Cronin M, Fowler M, Pritzker M. Morphological characteristics of catalyst layer defects in catalyst-coated membranes in PEM fuel cells. Electrochemistry (Tokyo, Jpn) 2023;4(1):1–20. https://doi.org/10.3390/electrochem4010001.
[12] Qin Y, Ma S, Chang Y, Liu Y, Yin Y, Zhang J, et al. Modeling the membrane/CL delamination with the existence of CL crack under RH cycling conditions of PEM fuel cell. Int J Hydrogen Energy 2021;46(12):8722–35. https://doi.org/10.1016/j.ijhydene.2020.12.043.
[13] Ma S, Qin Y, Liu Y, Sun L, Guo Q, Yin Y. Delamination evolution of PEM fuel cell membrane/CL interface under asymmetric RH cycling and CL crack location. Appl Energy 2022;310:118551. https://doi.org/10.1016/j.apenergy.2022.118551.
[14] Weber AZ. Gas-crossover and membrane-Pinhole effects in polymer-electrolyte fuel cells. J Electrochem Soc 2008;155(6):B521. https://doi.org/10.1149/1.2898130.
[15] Halter J, Marone F, Schmidt TJ, Büchi FN. Breaking through the cracks: on the mechanism of phosphoric acid migration in high temperature polymer electrolyte fuel cells. J Electrochem Soc 2018;165(14):F1176–83. https://doi.org/10.1149/2.0501814jes.
[16] Bevilacqua N, George MG, Galbiati S, Bazylak A, Zeis R. Phosphoric acid Invasion in high temperature PEM fuel cell gas diffusion layers. Electrochim Acta 2017;257:89–98. https://doi.org/10.1016/j.electacta.2017.10.054.
[17] Shi J, Zhan Z, Zhang Di, Yu Y, Yang X, He L, et al. Effects of cracks on the mass transfer of polymer electrolyte membrane fuel cell with high performance membrane electrode assembly. J Wuhan Univ Technol -Materials Sci Ed 2021;36(3):318–30. https://doi.org/10.1007/s11595-021-2412-z.
[18] Zhang J, Bai H, Yan W, Zhang J, Wang H, Xiang Y, et al. Enhancing cell performance and durability of high temperature polymer electrolyte membrane fuel cells by inhibiting the formation of cracks in catalyst layers. J Electrochem Soc 2020;167(11):114501. https://doi.org/10.1149/1945-7111/ab9fe0.
[19] Cui L, Zhang J, Sun Y, Lu S, Xiang Y. Effect of addition of carbon nanotubes on the performance of a low Pt loading membrane-electrode-assembly in proton exchange membrane fuel cells. Hua Hsueh Hsueh Pao 2019;77(1):47. https://doi.org/10.6023/A18080344.
[20] Eatemadi A, Daraee H, Karimkhanloo H, Kouhi M, Zarghami N, Akbarzadeh A, et al. Carbon nanotubes: properties, synthesis, purification, and medical applications. Nanoscale Res Lett 2014;9(1):393. https://doi.org/10.1186/1556-276X-9-393.
[21] Popov VN. Carbon nanotubes: properties and application. Mater Sci Eng R Rep 2004;43(3):61–102. https://doi.org/10.1016/j.mser.2003.10.001.
[22] Gupta N, Gupta SM, Sharma SK. Carbon nanotubes: synthesis, properties and engineering applications. Carbon Lett 2019;29(5):419–47. https://doi.org/10.1007/s42823-019-00068-2.
[23] Luo C, Xie H, Wang Q, Luo G, Liu C. A review of the application and performance of carbon nanotubes in fuel cells. J Nanomater 2015;2015(7):1–10. https://doi.org/10.1155/2015/560392.
[24] Scherer GW. Theory of drying. J Am Ceram Soc 1990;73(1):3–14. https://doi.org/10.1111/j.1151-2916.1990.tb05082.x.
[25] Suzuki T, Hashizume R, Hayase M. Effect of blending carbon nanoparticles and nanotubes on the formation of porous structure and the performance of proton exchange membrane fuel cell. J Power Sources 2015;286. https://doi.org/10.1016/j.jpowsour.2015.03.119. 15 July 2015):109–17.
[26] Griffith AA. VI. The phenomena of rupture and flow in solids. Phil Trans Roy Soc Lond 1921;221(582–593):163–98. https://doi.org/10.1098/rsta.1921.0006.
[27] Tirumkudulu MS, Russel WB. Cracking in drying latex films. Langmuir 2005;21(11):4938–48. https://doi.org/10.1021/la048298k.
[28] Singh KB, Deoghare G, Tirumkudulu MS. Cracking in soft-hard latex blends: theory and experiments. Langmuir 2009;25(2):751–60. https://doi.org/10.1021/la802857q.
[29] Kumano N, Kudo K, Suda A, Akimoto Y, Ishii M, Nakamura H. Controlling cracking formation in fuel cell catalyst layers. J Power Sources 2019;419:219–28. https://doi.org/10.1016/j.jpowsour.2019.02.058.
[30] Hoffmann E, Zhang S, Thoma M, Damm C, Peukert W. Formulation of carbon black-ionomer dispersions for thin film formation in fuel cells. Particuology 2019;44:7–21. https://doi.org/10.1016/j.partic.2018.08.001.
[31] Du S, Guan S, Mehrazi S, Zhou F, Pan M, Zhang R, et al. Effect of dispersion method and catalyst on the crack morphology and performance of catalyst layer of PEMFC. J Electrochem Soc 2021;168(11):114506. https://doi.org/10.1149/1945-7111/ac3598.
[32] Xu W, Scott K. The effects of ionomer content on PEM water electrolyser membrane electrode assembly performance. Int J Hydrogen Energy 2010;35(21):12029–37. https://doi.org/10.1016/j.ijhydene.2010.08.055.
[33] Huang D-C, Yu P-J, Liu F-J, Huang S-L, Hsueh K-L. Effect of dispersion solvent in catalyst ink on proton exchange membrane fuel cell performance. Int J Electrochem Sci 2011;(6):2551–65.
[34] Therdthianwong A, Ekdharmasuit P, Therdthianwong S. Fabrication and performance of membrane electrode assembly prepared by a catalyst-coated membrane method: effect of solvents used in a catalyst ink mixture. Energy Fuels 2010;24(2):1191–6. https://doi.org/10.1021/ef901105k.
[35] Hasegawa N, Kamiya A, Matsunaga T, Kitano N, Harada M. Analysis of crack formation during fuel cell catalyst ink drying process. Reduction of catalyst layer cracking by addition of high boiling point solvent. Colloids Surf A Physicochem Eng Asp 2021;628:127153. https://doi.org/10.1016/j.colsurfa.2021.127153.
[36] Baez-Cotto CM, Pfeilsticker JP, Godoy AO, Batool M, Zaccarine S, Wang M, et al. The effect of ink ball milling time on interparticle interactions and ink microstructure and their influence on crack formation in rod-coated catalyst layers.

J Power Sources 2023;583:233567. https://doi.org/10.1016/j.jpowsour.2023.233567.
[37] Scheepers F, Stähler A, Stähler M, Carmo M, Lehnert W, Stolten D. Layer Formation from polymer carbon-black dispersions. Coatings 2018;8(12):450. https://doi.org/10.3390/coatings8120450.
[38] Scheepers F, Stähler A, Stähler M, Carmo M, Lehnert W, Stolten D. Steering and in situ monitoring of drying phenomena during film fabrication. J Coating Technol Res 2019;1–9. https://doi.org/10.1007/s11998-019-00206-5.
[39] Stagg BJ, Charalampopoulos TT. Refractive indices of pyrolytic graphite, amorphous carbon, and flame soot in the temperature range 25° to 600°C. Combust Flame 1993;94(4):381–96. https://doi.org/10.1016/0010-2180(93)90121-I.
[40] Klemens J, Schneider L, Burger D, Zimmerer N, Müller M, Bauer W, et al. Process and drying behavior toward higher drying rates of hard carbon anodes for sodium-ion batteries with different particle sizes: an experimental study in comparison to graphite for lithium-ion-batteries. Energy Technol 2023;11(8). https://doi.org/10.1002/ente.202300338.
[41] Klemens J, Schneider L, Herbst EC, Bohn N, Müller M, Bauer W, et al. Drying of NCM cathode electrodes with porous, nanostructured particles versus compact solid particles: comparative study of binder migration as a function of drying conditions. Energy Technol 2022;10(4):2100985. https://doi.org/10.1002/ente.202100985.
[42] Kumberg J, Bauer W, Schmatz J, Diehm R, Tönsmann M, Müller M, et al. Reduced drying time of anodes for lithium-ion batteries through simultaneous multilayer coating. Energy Technol 2021;9(10):2100367. https://doi.org/10.1002/ente.202100367.
[43] Kumberg J, Baunach M, Eser JC, Altvater A, Scharfer P, Schabel W. Investigation of drying curves of lithium-ion battery electrodes with a new gravimetrical double-side batch dryer concept including setup characterization and model simulations. Energy Technol 2021;9(2):2000889. https://doi.org/10.1002/ente.202000889.
[44] Kumberg J, Müller M, Diehm R, Spiegel S, Wachsmann C, Bauer W, et al. Drying of lithium-ion battery anodes for use in high-energy cells: influence of electrode thickness on drying time, adhesion, and crack formation. Energy Technol 2019;7(11):1900722. https://doi.org/10.1002/ente.201900722.
[45] Jaiser S, Friske A, Baunach M, Scharfer P, Schabel W. Development of a three-stage drying profile based on characteristic drying stages for lithium-ion battery anodes. Dry Technol 2017;35(10):1266–75. https://doi.org/10.1080/07373937.2016.1248975.
[46] Jaiser S, Sanchez Salach N, Baunach M, Scharfer P, Schabel W. Impact of drying conditions and wet film properties on adhesion and film solidification of lithium-ion battery anodes. Dry Technol 2017;35(15):1807–17. https://doi.org/10.1080/07373937.2016.1276584.
[47] Jaiser S, Funk L, Baunach M, Scharfer P, Schabel W. Experimental investigation into battery electrode surfaces: the distribution of liquid at the surface and the emptying of pores during drying. J Colloid Interface Sci 2017;494:22–31. https://doi.org/10.1016/j.jcis.2017.01.063.
[48] Jaiser S, Müller M, Baunach M, Bauer W, Scharfer P, Schabel W. Investigation of film solidification and binder migration during drying of Li-Ion battery anodes. J Power Sources 2016;318:210–9. https://doi.org/10.1016/j.jpowsour.2016.04.018.
[49] Baunach M, Jaiser S, Schmelzle S, Nirschl H, Scharfer P, Schabel W. Delamination behavior of lithium-ion battery anodes: influence of drying temperature during electrode processing. Dry Technol 2016;34(4):462–73. https://doi.org/10.1080/07373937.2015.1060497.
[50] Baunach M, Jaiser S, Cavadini P, Scharfer P, Schabel W. Local heat transfer characteristics of a slot nozzle array for batch drying of thin films under industrial process conditions. J Coating Technol Res 2015;12(5):915–20. https://doi.org/10.1007/s11998-015-9712-1.
[51] Schneider L, Klemens J, Herbst EC, Müller M, Scharfer P, Schabel W, et al. Transport properties in electrodes for lithium-ion batteries: comparison of compact versus porous NCM particles. J Electrochem Soc 2022;169(10):100553. https://doi.org/10.1149/1945-7111/ac9c37.
[52] Klemens J, Burger D, Schneider L, Spiegel S, Müller M, Bohn N, et al. Drying of compact and porous NCM cathode electrodes in different multilayer architectures: influence of layer configuration and drying rate on electrode properties. Energy Technol 2023;11(8). https://doi.org/10.1002/ente.202300267.
[53] Sigma-Aldrich. Product specification carbon nanotube, multi-walled. May 12, 2023. Available from: https://www.sigmaaldrich.com/specification-sheets/369/935/901019-BULK____ALDRICH_.pdf.
[54] Bohn L, Holst M von, Ortiz EC, Breitwieser M, Vierrath S, Klose C. Methods— a simple method to measure in-plane electrical resistance of PEM fuel cell and electrolyzer catalyst layers. J Electrochem Soc 2022;169(5):54518. https://doi.org/10.1149/1945-7111/ac6e09.
[55] Altvater A, Heckmann T, Eser JC, Spiegel S, Scharfer P, Schabel W. (Near-) infrared drying of lithium-ion battery electrodes: influence of energy input on process speed and electrode adhesion. Energy Technol 2023;11(5). https://doi.org/10.1002/ente.202200785.
[56] Klemens J, Wurba A-K, Burger D, Müller M, Bauer W, Büchele S, et al. Challenges and opportunities for large-scale electrode processing for sodium-ion and lithium-ion battery. Batteries & Supercaps 2023;6(11). https://doi.org/10.1002/batt.202300291.